

# Experimental Realization of Atomic Monolayer Si<sub>9</sub>C<sub>15</sub>

Zhao-Yan Gao, Wenpeng Xu, Yixuan Gao, Roger Guzman, Hui Guo, Xueyan Wang, Qi Zheng, Zhili Zhu, Yu-Yang Zhang, Xiao Lin, Qing Huan, Geng Li,\* Lizhi Zhang,\* Wu Zhou,\* and Hong-Jun Gao\*

Monolayer Si<sub>x</sub>C<sub>y</sub> constitutes an important family of 2D materials that is predicted to feature a honeycomb structure and appreciable bandgaps. However, due to its binary chemical nature and the lack of bulk polymorphs with a layered structure, the fabrication of such materials has so far been challenging. Here, the synthesis of atomic monolayer Si<sub>9</sub>C<sub>15</sub> on Ru (0001) and Rh(111) substrates is reported. A combination of scanning tunneling microscopy (STM), X-ray photoelectron spectroscopy (XPS), scanning transmission electron microscopy (STEM), and density functional theory (DFT) calculations is used to infer that the 2D lattice of Si<sub>9</sub>C<sub>15</sub> is a buckled honeycomb structure. Monolayer Si<sub>9</sub>C<sub>15</sub> shows semiconducting behavior with a bandgap of ≈1.9 eV. Remarkably, the Si<sub>9</sub>C<sub>15</sub> lattice remains intact after exposure to ambient conditions, indicating good air stability. The present work expands the 2D-materials library and provides a promising platform for future studies in nanoelectronics and nanophotonics.

that another kind of 2D materials, which does not have layered bulk counterparts, can be synthesized by epitaxial growth on proper substrates.<sup>[3,4]</sup> Silicene,<sup>[5,6]</sup> borophene,<sup>[7,8]</sup> germanene,<sup>[9]</sup> stanene,<sup>[10]</sup> and bismuthene<sup>[11]</sup> are some examples. This technique further expanded the 2D family. However, despite the many achievements in fabricating new 2D materials, 2D Si<sub>x</sub>C<sub>y</sub>, a class of materials that have been predicted and studied theoretically,<sup>[12,13]</sup> have yet to be fabricated.<sup>[14]</sup>

Having a crystal structure similar to silicon and diamond, bulk silicon carbide cannot serve as the parent of a 2D counterpart for mechanical exfoliation. As a result, although theorists have predicted various Si<sub>x</sub>C<sub>y</sub> monolayers with fascinating physical

properties,<sup>[12,13,15,16]</sup> experimental progress is limited. Flakes of quasi-2D SiC and SiC<sub>2</sub> were fabricated by Lin et al. through the reaction of exfoliated graphene and silicon.<sup>[17]</sup> Nevertheless, these flakes are not atomically thin and their thickness cannot be well controlled. Susi et al. reported the formation of atomically thin 2D SiC nanograins within graphene lattice induced by the electron beam of a scanning transmission electron microscope. The obtained grains are less than one nanometer in size.<sup>[16]</sup> Recently, Chabi et al. fabricated micrometre-scale 2D silicon carbide flakes by a liquid exfoliation method.<sup>[18]</sup> However, scalable experimental techniques for fabricating large-scale monolayer silicon carbide are still lacking.

Herein, we report the synthesis of high-quality, large-scale atomic monolayer Si<sub>9</sub>C<sub>15</sub> on Ru (0001) and Rh(111) substrates. First, a graphene layer is grown on a Ru(0001) or Rh(111) substrate. Silicon atoms are then evaporated onto the graphene surface, followed by high-temperature annealing to activate the reaction between Si and graphene to form the Si<sub>9</sub>C<sub>15</sub> layer. This novel 2D material exhibits semiconducting behavior with a bandgap of ≈ 1.9 eV. Monolayer Si<sub>9</sub>C<sub>15</sub> shows good environmental stability, with no significant change in lattice structure and electronic properties after direct exposure to air for 72 h.

## 1. Introduction

The exfoliation of graphene from graphite in 2004<sup>[1,2]</sup> opened up an era of 2D materials. Since then, many 2D materials have been successfully fabricated by exfoliating or by thinning their corresponding layered bulks. Later, researchers realized


Z.-Y. Gao, W. Xu, Y. Gao, H. Guo, X. Wang, Q. Zheng, Z. Zhu, X. Lin, Q. Huan, G. Li, H.-J. Gao  
Beijing National Laboratory for Condensed Matter Physics and Institute of Physics  
Chinese Academy of Sciences  
Beijing 100190, China  
E-mail: gengli.iop@iphy.ac.cn; hjgao@iphy.ac.cn

Z.-Y. Gao, W. Xu, Y. Gao, R. Guzman, H. Guo, X. Wang, Q. Zheng, Z. Zhu, Y.-Y. Zhang, X. Lin, Q. Huan, G. Li, L. Zhang, W. Zhou, H.-J. Gao  
School of Physical Sciences and CAS Key Laboratory of Vacuum Physics  
University of Chinese Academy of Sciences  
Beijing 100190, China  
E-mail: zhanglz@nanoctr.cn; wuzhou@ucas.ac.cn

Y. Gao, G. Li, H.-J. Gao  
Songshan Lake Materials Laboratory  
Dongguan, Guangdong 523808, China

Y.-Y. Zhang, X. Lin, G. Li, W. Zhou, H.-J. Gao  
CAS Center for Excellence in Topological Quantum Computation  
University of Chinese Academy of Sciences  
Beijing 100190, China

L. Zhang  
National Center for Nanoscience and Technology  
Chinese Academy of Sciences  
Beijing 100190, China

 The ORCID identification number(s) for the author(s) of this article can be found under <https://doi.org/10.1002/adma.202204779>.

DOI: 10.1002/adma.202204779

## 2. Results

### 2.1. Formation of Monolayer Si<sub>x</sub>C<sub>y</sub> on Ru(0001) and Rh(111) Surfaces

Similar to silicon, bulk silicon carbide is not a van der Waals layered material, whereby exfoliation of large-scale monolayer

silicon carbide from the bulk material would be difficult. The Ru(0001) substrate has proven to be a good template for epitaxial growth of both graphene and silicene.<sup>[19,20]</sup> We therefore start with monolayer graphene grown epitaxially on a Ru(0001) substrate (G/Ru). Due to strong interactions between graphene and the Ru substrate, a long-range moiré structure is formed (Figure 1a,b). The single crystalline nature of the graphene layer (Figure 1c) makes it a good template to fabricate 2D  $\text{Si}_x\text{C}_y$ . Inspired by the fact that Si intercalation between the graphene and the Ru substrate creates vacancy defects in the graphene lattice,<sup>[21]</sup> we adopted a modified intercalation strategy to construct the  $\text{Si}_x\text{C}_y$  layer. Three atomic layers of Si atoms were evaporated onto the G/Ru surface, and the sample was annealed at 1400 K for 4 min.

After the annealing, a new honeycomb structure was obtained (Figure 1d,e). This new structure shows flattened geometry compared with the corrugated graphene, with a periodicity of  $\approx 1$  nm (Figure S1, Supporting Information). The white blobs on the surface are likely Si clusters formed by excessive Si atoms, bonding randomly to the defected sites of the  $\text{Si}_x\text{C}_y$

layer (Figure 1e). Low energy electron diffraction (LEED) analysis verifies that the graphene layer is completely gone and a new  $(2\sqrt{3} \times 2\sqrt{3})R30^\circ$  super-structure with respect to the Ru lattice appears across the whole sample surface (Figure 1f), consistent with the scanning tunneling microscopy (STM) result (Figure 1e). The sharp diffraction spots suggest the formation of a highly ordered 2D structure, spanning across the entire substrate surface. Remarkably, the same 2D structure can also be grown on the surface of Rh(111), which possesses similar lattice constants and catalytic properties to those of Ru(0001).<sup>[22,23]</sup> We note that the size of the 2D layer extends out of the scope of our STM scanner (Figure S2, Supporting Information), which is larger than  $1.2 \times 1.2 \mu\text{m}^2$ .

The chemical composition of the 2D layer on Ru was probed by X-ray photoelectron spectroscopy (XPS) measurements (Figure S3, Supporting Information). As expected, the XPS data shows strong signals of Ru, Si, and C. It has been previously reported that surface metal atoms may interact strongly with the overlying 2D material<sup>[24]</sup> and even participate in forming 2D surface alloys,<sup>[25]</sup> leading to a significant shift or splitting of the

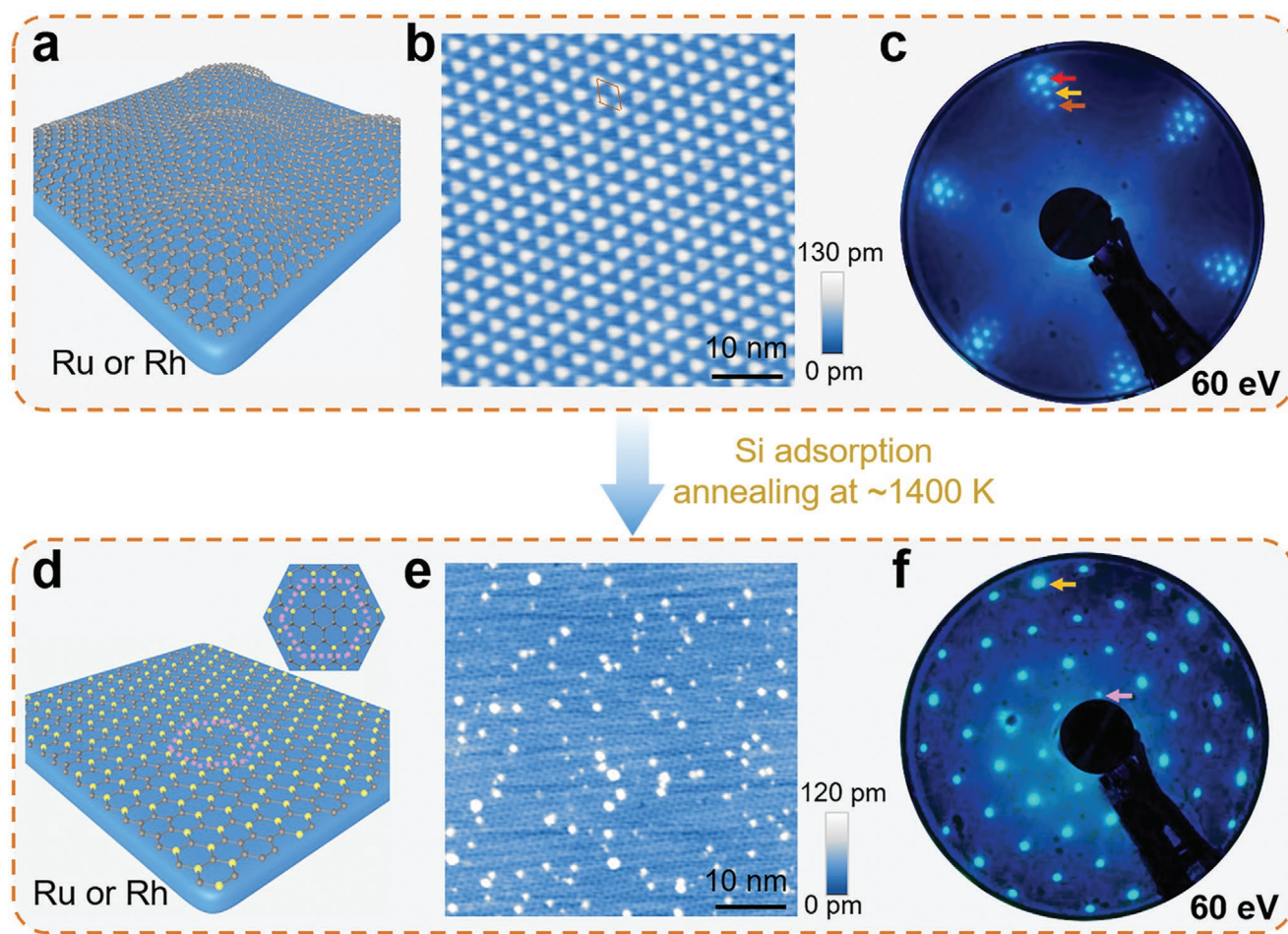


**Figure 1.** Monolayer  $\text{Si}_x\text{C}_y$  formed on Ru(0001) and Rh(111) substrate. a–c) Schematic drawing of monolayer graphene on Ru(0001) or Rh(111) (a), STM image (b) ( $V_s = -1$  V,  $I_t = 50$  pA), and LEED pattern (c) of monolayer graphene on Ru(0001). The unit cell of the moiré pattern is highlighted by an orange rhombus. The diffraction spots of graphene, Ru, and the graphene/Ru moiré pattern are indicated by the red, yellow and orange arrows, respectively. d–f) Schematic drawing of monolayer  $\text{Si}_x\text{C}_y$  on Ru(0001) or Rh(111) (d), STM image (e) ( $V_s = -1$  V,  $I_t = 50$  pA), and LEED pattern (f) of monolayer  $\text{Si}_x\text{C}_y$  on Ru(0001) after Si dosage. The diffraction spot of the  $\text{Si}_x\text{C}_y$  layer is indicated by the pink arrow.



main peak in XPS spectra.<sup>[26,27]</sup> In our case, the Ru 3d<sub>5/2</sub> core level spectrum shows a single, non-splitting peak at 280.13 eV (Figure S3b, Supporting Information), comparable to that in the G/Ru system (280.06 eV, Figure S3a, Supporting Information). As a result, the possibility that Ru atoms are involved in the 2D layer as an alloy can be ruled out. The core-level spectra of Si 2p and C 1s indicate the presence of Si and C atoms that are not in their elemental states, suggesting the formation of a Si<sub>x</sub>C<sub>y</sub> layer.

## 2.2. Atomic Structure of the Si<sub>x</sub>C<sub>y</sub> Layer

Having determined the chemical constituents of the 2D layer, we then performed detailed STM characterization to determine the atomic structure. A honeycomb lattice of Si<sub>x</sub>C<sub>y</sub> on Ru(0001) substrate is clearly resolved under negative sample bias (Figure 2a). However, under positive bias (Figure S4a, Supporting Information), the local density of states (LDOS) at the centers of the honeycomb become visible and the STM image changes to a hexagonal pattern. The transition is more evident in the bias-dependent STM images (Figure S5, Supporting Information). This observation suggests that the central sites of the honeycomb may have different atomic configurations and hence electronic structures compared with the regions at the vertices of the honeycomb. The conclusion is further

corroborated by the atomic force microscopy (AFM) results where the vertices are higher than the central sites of the honeycomb (Figure S6, Supporting Information).

Atomically resolved STM images show that each vertex of the honeycomb structure consists of three bright spots, forming an upward triangle (left panel in Figure 2c), while the center has one downward triangle (left panel in Figure S4b, Supporting Information). The triangle structure is reminiscent of epitaxial silicene, in which only three out of six Si atoms in a hexagon buckle outward of the substrate and can be captured by STM, forming a triangle shape.<sup>[5]</sup> We further identified that the distance between the bright spots in an upward triangle (downward triangle) is  $\approx 3.0$  Å (2.3 Å), approximately  $\sqrt{3}$  times the length of Si–C (C–C) bond.<sup>[16,28]</sup> We, therefore, constructed an atomic model by placing Si–C hexagons at the vertices and C–C hexagons at the centers of the honeycomb. After considering all possible configurations by density functional theory (DFT) calculations, we determined the energetically most stable structure, as shown in Figure 2b. The optimized 2D structure consists of Si and C atoms, with a stoichiometric formula of Si<sub>9</sub>C<sub>15</sub>.

Each C–C hexagon is surrounded by twelve Si–C hexagons, as outlined by the pink dashed hexagons in Figure 2b. In the Si–C hexagons, the Si atoms (yellow spheres) preferentially sit at hollow sites of the Ru substrate due to larger binding energy compared with the top sites,<sup>[20]</sup> while the C atoms (dark grey

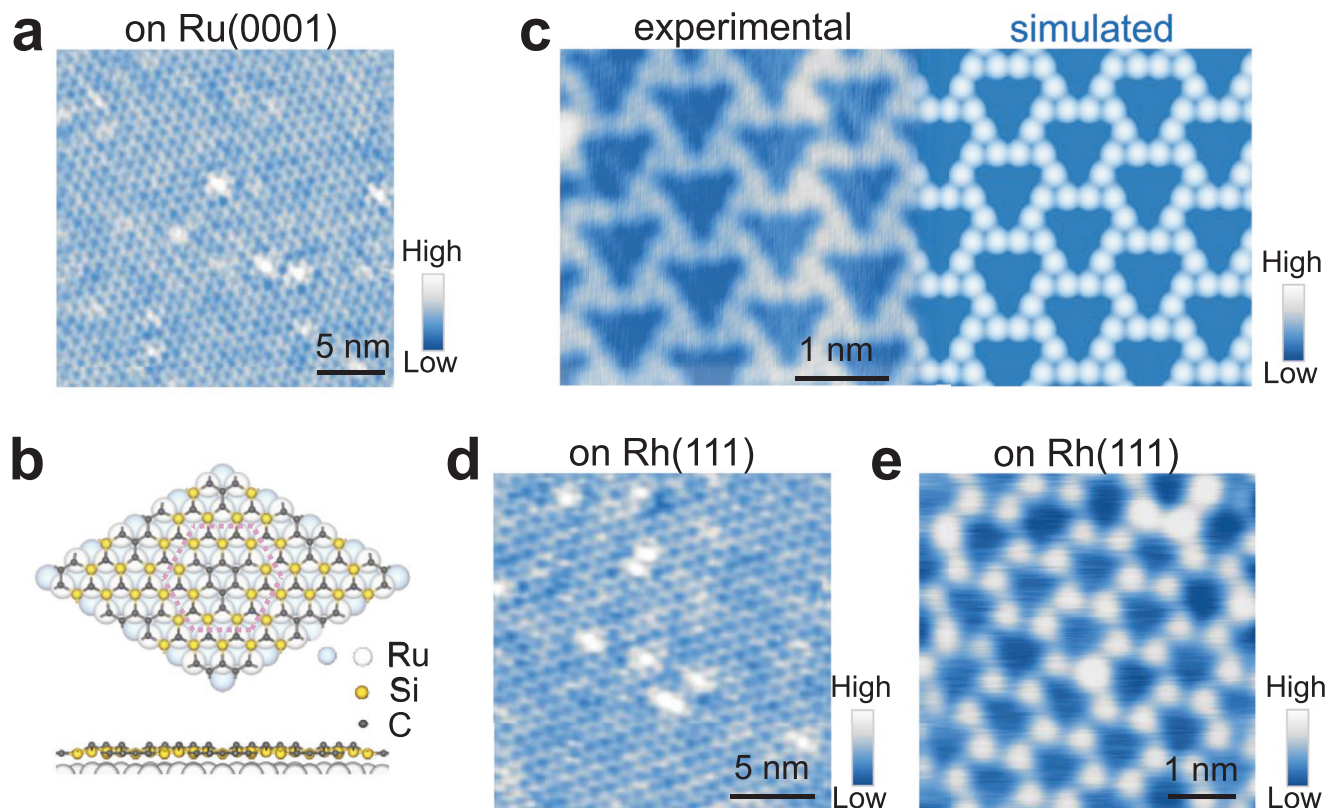


**Figure 2.** Atomic structure of the Si<sub>9</sub>C<sub>15</sub> layer on Ru and Rh. a) STM topographic image of Si<sub>9</sub>C<sub>15</sub> on Ru surface under  $-1$  V ( $I_t = 50$  pA). b) Top and side views of the relaxed atomic model showing the buckle geometry of Si<sub>9</sub>C<sub>15</sub>. c) High-resolution STM image of the monolayer Si<sub>9</sub>C<sub>15</sub> on Ru surface showing the atomic arrangement under  $-1$  V (left panel), and the corresponding simulated STM image (right panel) based on the configuration in (b). d, e) Large-scale (d) and high-resolution (e) STM images of the monolayer Si<sub>9</sub>C<sub>15</sub> on Rh(111) under  $-0.2$  V ( $I_t = 1$  nA).

spheres) are located on top sites. As a result, the three C atoms buckle outward of the Ru substrate, giving rise to the triangular structure in STM images. In the C–C hexagon, due to the buckled atomic arrangement of  $sp^3/sp^2$ -like hybridized Si atoms, the C atoms connecting to Si are slightly lower than the ones connecting to the C atoms (Figure S7, Supporting Information), contributing to the downward triangles. The transition from honeycomb to hexagonal geometry in STM images is attributed to a smaller difference in the LDOS between the C atoms in the C–C hexagon and that in the Si–C hexagon under positive sample bias voltages (Figure S8a,b, Supporting Information).

Corresponding STM simulations based on the proposed model with a sample bias of  $-1$  (right panel in Figure 2c) and  $+1$  V (right panel in Figure S4b, Supporting Information) agree well with the experimental STM images (left panels in Figure 2c and Figure S4b, Supporting Information). We note that the Si–C hexagons are not perfectly aligned, but slightly rotated with respect to each other due to interaction with the substrate. This feature is also in excellent agreement with the slightly rotated upward triangles in the STM images (left panels in Figure 2c and Figure S4b, Supporting Information). In contrast to the case of  $Si_9C_{15}$  on Ru(0001) as discussed above, the STM images of  $Si_9C_{15}$  on Rh(111) show no obvious change

under negative and positive voltages (Figure 2d,e and Figure S9, Supporting Information). STM simulations using the same atomic configuration on Rh also show good agreement with the experimental results (Figure S9, Supporting Information).

In order to further confirm the proposed atomic structural model of  $Si_9C_{15}$ , we performed cross-sectional scanning transmission electron microscopy (STEM) experiments of monolayer  $Si_9C_{15}$  grown on Rh and Ru substrates. The topmost layers in the simultaneously acquired high-angle annular dark-field (HAADF, upper panel in Figure 3a) and annular bright-field (ABF, lower panel in Figure 3a) images are assigned to the  $Si_9C_{15}$ , lying on top of an Rh(111) substrate. The electron beam is incident along the zigzag direction of the honeycomb lattice of  $Si_9C_{15}$ , and both images show good agreement with the simulated results based on our proposed  $Si_9C_{15}$  model (right panels in Figure 3a). Notice that, due to the low scattering cross-section of electrons with light atoms, the C columns are only visible in the ABF images. ABF intensity line profiles taken from the experimental and simulated images illustrate the distribution of the Rh, Si, and C atoms (Figure 3b) across the monolayer/metal interface along the orange dashed arrow in Figure 3a. The excellent agreement between the experimental and simulated images, thus confirms the formation of the buckled structure of  $Si_9C_{15}$  on Rh(111). STEM results from the sample grown on a Ru(0001) substrate,

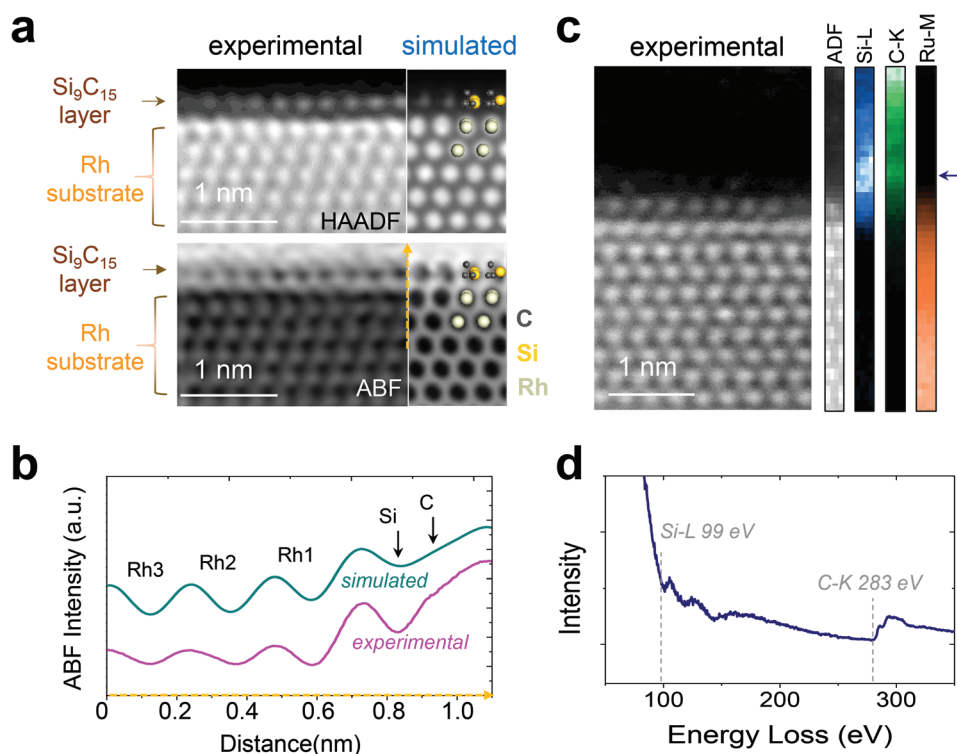


**Figure 3.** Cross-sectional STEM analysis of the monolayer  $Si_9C_{15}$ . a) A set of simultaneously acquired STEM-HAADF (top) and ABF (bottom) images of the  $Si_9C_{15}$  monolayer on Rh(111) seen along the zigzag direction. The right-hand-side panels are the corresponding image simulations computed using the relaxed atomic model. The atomic model is overlaid on the images suggesting the formation of the  $Si_9C_{15}$  structure. b) ABF intensity line profiles taken from the experimental and simulated images in (a), showing the distribution of the Rh, Si, and C atoms across the interface along the orange dashed arrow. The profiles were integrated over a region of 1 nm in width. c) HAADF image of the  $Si_9C_{15}$  monolayer on Ru(0001) seen along the zigzag direction (left) and EELS chemical mapping of the Si–L, C–K, and Ru–M edges (right). The EELS mappings were acquired simultaneously with the ADF image across the monolayer–substrate interface, showing the elemental distribution. The mapping was acquired with the electron beam scanning from the Ru substrate into the  $C_{60}$  capping layer. d) Electron energy loss spectrum extracted from the  $Si_9C_{15}$  monolayer (blue arrow in (c)) showing the Si–L and C–K edges.

viewed along the armchair direction of the honeycomb lattice, leading to the same conclusion that the buckled structure of Si<sub>9</sub>C<sub>15</sub> is present (Figure S10, Supporting Information).

To verify that the topmost layer indeed consists of Si and C atoms, we performed atomic-layer-resolution electron energy loss spectroscopy (EELS) analysis. The left panel of Figure 3c shows a STEM-HAADF image of the Si<sub>9</sub>C<sub>15</sub> monolayer grown on Ru(0001), imaged along the zigzag direction. The EELS chemical mapping taken on this sample (right panel in Figure 3c) shows a pronounced signal of the Si and C on the surface of the Ru(0001) substrate. Note that due to the presence of surface steps on the Ru(0001) substrate and the electron beam induced damage to the Si<sub>9</sub>C<sub>15</sub> monolayer, the Si signal extends slightly into the C<sub>60</sub> protecting layer (see Experimental Section). Nevertheless, both the Si and C signals display strong enhancement within an atomic-layer on the Ru surface, as confirmed by the electron energy loss spectrum in Figure 3d. The stronger C signal away from the Ru surface comes from the C<sub>60</sub> protecting layer (see Experimental Section). Our combined STM, XPS, AFM, STEM, and DFT studies unambiguously determine the buckled honeycomb structure of Si<sub>9</sub>C<sub>15</sub>.

### 2.3. Formation Mechanism of Si<sub>9</sub>C<sub>15</sub>

Compared with the Si intercalation process,<sup>[21]</sup> higher dosage of Si as well as higher annealing temperature were used in order to create a large number of vacancy defects in graphene. These defects cannot be timely repaired by the carbon atoms in the metal substrate, leaving active sites that are able to react with the Si atoms under high temperatures. The reaction process transforms the graphene layer into a dynamically stable Si<sub>9</sub>C<sub>15</sub> layer. To corroborate this formation mechanism, we intentionally decreased the Si dosage and found boundaries between Si<sub>9</sub>C<sub>15</sub> and graphene (Figure S11, Supporting Information). The graphene layer seems fractured with a large number of cracks and defects (Figure S11a,c, Supporting Information), suggesting that the created defects in the graphene layer cannot be healed by C atoms in the bulk Ru. These defects can, therefore, react with the excess Si atoms under high temperatures and finally transform into the dynamically stable Si<sub>9</sub>C<sub>15</sub> phase. We also found boundaries between a Si<sub>9</sub>C<sub>15</sub> island and partially Si intercalated graphene (Figure S11d, Supporting Information). A height profile along the black line in Figure S11e, Supporting Information, shows that the apparent height of the Si<sub>9</sub>C<sub>15</sub> island is comparable to that of the corrugated graphene, indicating that the as-fabricated Si<sub>9</sub>C<sub>15</sub> is a monolayer.

### 2.4. Electronic Structure and Edge States of Si<sub>9</sub>C<sub>15</sub> Islands

It has been predicted that the gap size of Si<sub>x</sub>C<sub>1-x</sub> varies as a function of *x*, driving the material from semimetallic to semiconducting.<sup>[15]</sup> Our DFT calculations show that the free-standing Si<sub>9</sub>C<sub>15</sub> layer is a direct-bandgap semiconductor with a gap size of 1.86 eV (Figure S12, Supporting Information). To identify the electronic structure of the monolayer on Ru, we performed scanning tunneling spectroscopy (STS). *dI/dV* spectra acquired at the vertex (red) and center (black) of the honeycomb

structure exhibit a gap-like feature with a size of  $1.92 \pm 0.06$  eV (Figure 4a). Interestingly, significant conductance is still present in the expected gap region, reflecting remnant metallic characteristics induced by the interaction between Si<sub>9</sub>C<sub>15</sub> and Ru(0001).<sup>[29–31]</sup> The onsets of the spectra (brown dashed lines) are assigned to the valence band maximum (VBM) and conduction band minimum (CBM), respectively. The extracted gap size agrees with the calculated bandgap of freestanding Si<sub>9</sub>C<sub>15</sub> (Figure 4a and Figure S12b, Supporting Information). A series of *dI/dV* curves (Figure 4b) along the dashed white arrow in the inset of Figure 4a further indicates a homogeneous gap feature across the Si<sub>9</sub>C<sub>15</sub> layer. The periodical modulation of the *dI/dV* intensity confirms the slight difference in LDOS between the center and the vertex sites.

The absence of a moiré structure between Si<sub>9</sub>C<sub>15</sub> and the metal substrates, as well as the slight rotations of the Si–C hexagons, suggest a relatively strong coupling between them. Indeed, the *dI/dV* spectrum shows a finite density of states inside the gap feature (Figure 4a), which is likely contributed by charge transfer from the substrate. Our DFT calculation results indeed show a clear signature of charge redistribution between the 2D layer and the substrate (Figure S13, Supporting Information).

Occasionally we observed nano-islands of a second layer (Figure S14, Supporting Information). It has been reported that the second layer of an island of epitaxially grown 2D materials acts as a near-freestanding layer due to the decoupling effect of the first layer.<sup>[32]</sup> The existence of the second layer suggests that Si<sub>9</sub>C<sub>15</sub> is a layered material and the top layer can in principle be exfoliated as a real freestanding layer. The second-layer islands also provide a promising platform to investigate the edge states, which prove important for tuning the physical properties of 2D materials.<sup>[11,33]</sup> The coexistence of Si–C and C–C hexagons reduces the crystal symmetry of Si<sub>9</sub>C<sub>15</sub> compared with graphene or silicene, giving rise to several distinct atomic terminations on the edge. By examining the atomic structure of Si<sub>9</sub>C<sub>15</sub>, we identified six possible types of armchair edges (AEs) in free-standing Si<sub>9</sub>C<sub>15</sub> islands (Figure S15, Supporting Information).

Two types of AEs (AE1 and AE2) and one type of zigzag edge (ZE) are observed in the Si<sub>9</sub>C<sub>15</sub> island in Figure 4c (the zoom-in image is shown in Figure S14b, Supporting Information). *dI/dV* spectra show an elevated LDOS inside the gap (Figure 4d) at the edges. The line-cut intensity plot of *dI/dV* spectra across an AE further confirms that the enhanced LDOS is spatially localized at edge sites (Figure 4e). The edge states are robust and continuous, with a slight difference in the intensity on different types of edges (Figure 4f).

## 3. Discussion

Many epitaxial 2D materials do not have good air stability,<sup>[34]</sup> or require special chemical treatment to stabilize,<sup>[35,36]</sup> limiting their practical applications. To test the stability of the Si<sub>9</sub>C<sub>15</sub> monolayer, we expose the as-prepared sample to ambient conditions for 72 h. Before exposure to air, the sample was characterized by LEED and STM (Figure 5a,d), revealing good sample quality. After air exposure, the Si<sub>9</sub>C<sub>15</sub> on Ru can hardly be resolved due to the adsorption of gas molecules on the surface,



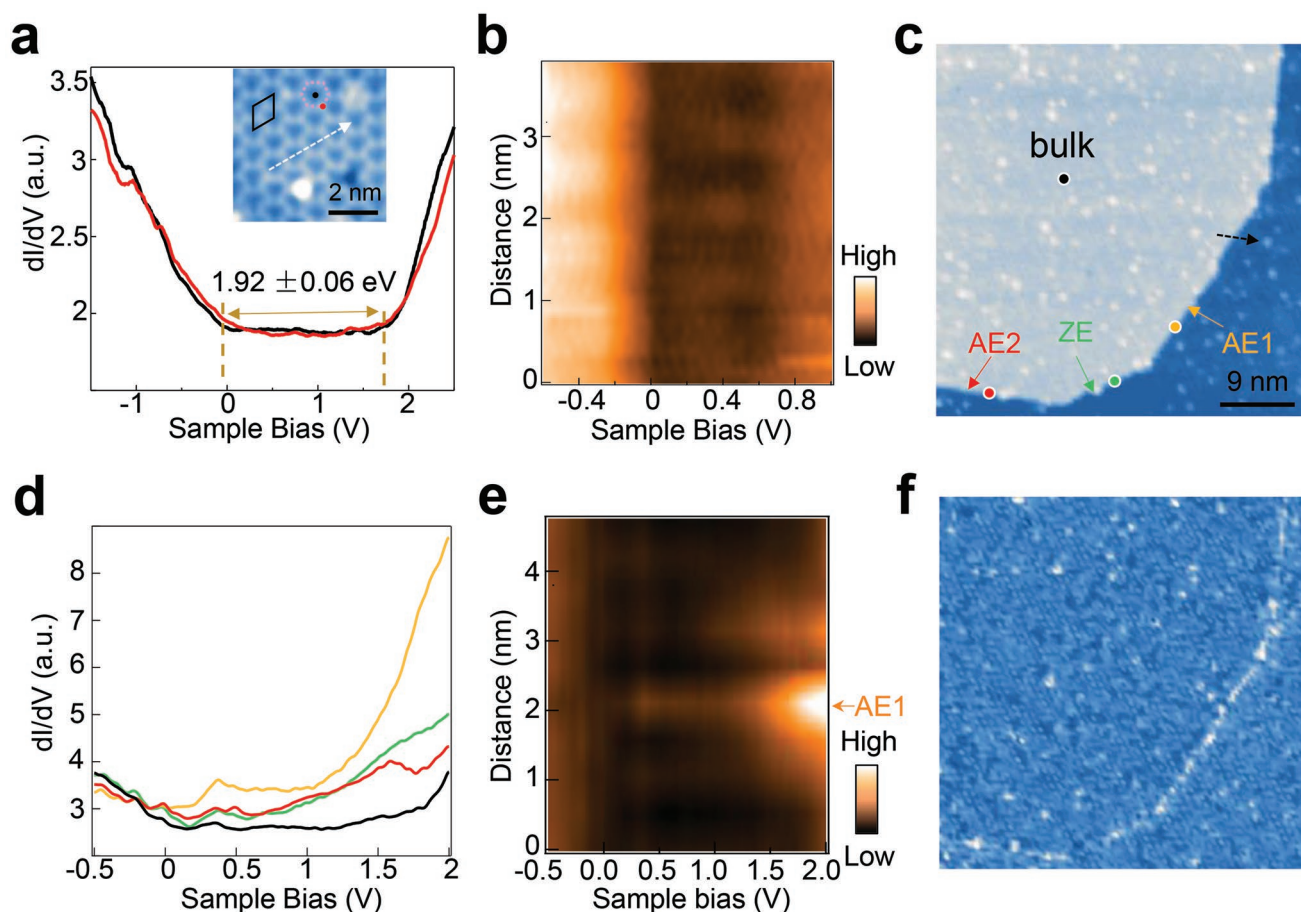


**Figure 4.** The electronic structure and edge states of  $\text{Si}_9\text{C}_{15}$ . a)  $dI/dV$  spectra measured at the vertex and center of the honeycomb lattice of  $\text{Si}_9\text{C}_{15}$ , as marked by red and black dots in the inset. The average value of the bandgap is determined to be  $1.92 \pm 0.06$  eV. b) Intensity plot of the spatial-dependent  $dI/dV$  spectra along the white dashed arrow in the inset of (a). c) STM topographic image showing a corner of a second-layer  $\text{Si}_9\text{C}_{15}$  island. The armchair (AE1 and AE2) and zigzag (ZE) type edge terminations are highlighted by colored arrows. d)  $dI/dV$  spectra taken at the edges as well as the interior of the  $\text{Si}_9\text{C}_{15}$  island, as highlighted by the colored dots in (c). e) Intensity plot of the spatial-dependent  $dI/dV$  spectra along the black dashed arrow in (c), showing the enhanced density of states at the edge. f)  $dI/dV$  map of (c) at 400 mV, showing enhanced density of states along the edge.

as shown in Figure 5b. We annealed the sample at 870 K for 1 h to remove possible physisorbed molecules. After annealing, the  $(2\sqrt{3} \times 2\sqrt{3})R30^\circ$  superstructure recovered in both LEED and STM images (Figure 5c,e). The blurred  $\sqrt{3}$  diffraction spots in the LEED pattern (Figure 5c) and the white impurities in the STM image are attributed to physically adsorbed oxygen molecules during the air exposure process. The results suggest that the  $\text{Si}_9\text{C}_{15}$  monolayers are relatively inert to air compared with the buckled silicene or germanene. The possible reason is that all Si atoms are buckled toward the Ru substrate, making them more difficult to react with the air molecules.

We also show the possibility of obtaining  $\text{Si}_x\text{C}_y$  layer with other Si:C ratio on different substrates by DFT calculation (Figure S16, Supporting Information). Compared with Ru or Rh, the metal substrates with smaller lattice constants favor lower Si:C ratio since the carbon hexagons are smaller than Si–C hexagons, while metal substrates with larger lattice constants favor higher Si:C ratio. Remarkably, 2D SiC layer is likely to form on the Au(111) surface. We note that the current growth strategy cannot be directly used for the Au substrate due to its low carbon solubility and melting temperature.

In summary, we have grown monolayer  $\text{Si}_9\text{C}_{15}$  on Ru(0001) and Rh(111) substrates. This new 2D material has a buckled honeycomb structure and a bandgap of  $\approx 1.9$  eV. Its reasonable air stability makes the ex situ process such as spectroscopic measurements and device fabrication possible. Like in many other epitaxially grown 2D structures, approaches to isolate the  $\text{Si}_9\text{C}_{15}$  layer from the metal substrates or to exfoliate it can expand its applications in the future.

#### 4. Experimental Section

**Sample Growth and Scanning Tunneling Microscopy/Spectroscopy:** The experiments were performed in a home-built low-temperature scanning probe microscope system<sup>[37]</sup> with a base pressure below  $2 \times 10^{-10}$  mbar. The Ru(0001) substrate was sputtered by  $\text{Ar}^+$  and then annealed under 1270 K to yield a clean surface. And the Rh(111) single crystal was cleaned by repeated cycles of  $\text{Ar}^+$  sputtering at room temperature, flash annealing to about 1400 K, annealing in an oxygen atmosphere at about 1050 K, and subsequent flash annealing in UHV to about 1400 K. Single-layer graphene was grown by exposing the Ru and Rh single crystal surface to ethylene at 1300<sup>[19]</sup> and at 1200 K,<sup>[22]</sup> respectively. Si atoms were evaporated from an E-beam evaporator and deposited

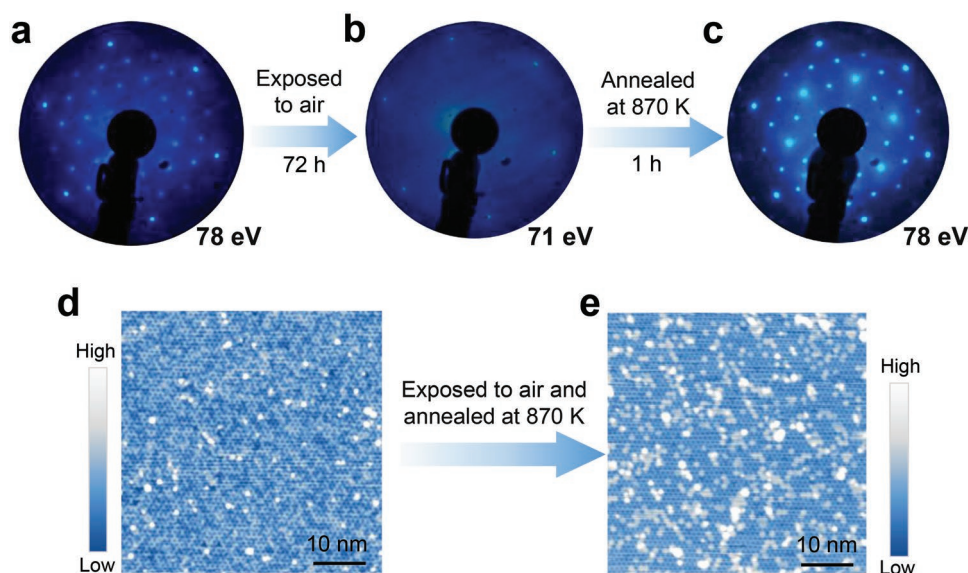


**Figure 5.** Air stability of the monolayer  $\text{Si}_9\text{C}_{15}$  on Ru. a) LEED pattern of monolayer  $\text{Si}_9\text{C}_{15}$  on Ru(0001) before exposed to air. b,c) LEED patterns of  $\text{Si}_9\text{C}_{15}$  on Ru(0001) taken before (b) and after (c) annealing after exposed to air for 72 h. d) STM image of monolayer  $\text{Si}_9\text{C}_{15}$  on Ru(0001) before exposed to air ( $V_s = -1$  V,  $I_t = 50$  pA). e) STM image of monolayer  $\text{Si}_9\text{C}_{15}$  on Ru(0001) after annealing after exposed to air. The honeycomb-like  $\text{Si}_9\text{C}_{15}$  lattice is preserved, showing good air stability ( $V_s = -1$  V,  $I_t = 50$  pA).

on G/Ru (G/Rh) substrate held at room temperature. The evaporation rate was calibrated to be  $0.33$  ML  $\text{minute}^{-1}$ . Subsequently, the sample was annealed to  $1400$  K ( $1300$  K) to initiate the growth of  $\text{Si}_9\text{C}_{15}$ . The STM images were acquired in the constant-current mode, using an electrochemically etched tungsten tip. All voltages were applied to the sample with respect to the tip. STS was acquired with a bias modulation of  $20$  mV at  $861.3$  Hz.

**X-ray Photoelectron Spectroscopy Measurements:** XPS measurements were performed at the photoelectron spectroscopy end-station of the Beijing Synchrotron Radiation Facility 4B9B beamline with a hemispherical energy analyzer. After growth, the samples were stored in a UHV suitcase and transferred to the XPS station for measuring their elementary composition. The Si-2p and C-1s core levels were collected using a photon energy of  $500$  eV. The photon energy was calibrated by measuring the Au-4f of a clean sheet of polycrystalline gold foil that was electrically connected to the sample. The samples were checked again by STM after the XPS experiments to guarantee that the quality and atomic structure of the  $\text{Si}_9\text{C}_{15}$  samples were well-protected during the whole transfer and measurement process.

**Density Functional Theory Calculations:** The calculations were carried out using Vienna ab initio simulation package (VASP).<sup>[38,39]</sup> The projected augmented wave (PAW) method was used to describe the core-valence interactions.<sup>[40]</sup> The generalized gradient approximation (GGA) in the form of Perdew–Burke–Ernzerhof (PBE) was adopted for the exchange–correlation functional.<sup>[41]</sup> Wave functions were expanded in a plane-wave basis set up to  $400$  eV energy cutoff. A slab model was used with six Ru layers as the substrate. The vacuum layer was larger than  $15$  Å. A  $\Gamma$ -centered  $12 \times 12 \times 1$  k-point sampling in the first Brillouin zone was used for the  $(2\sqrt{3} \times 2\sqrt{3})R30^\circ$  supercell. All atoms except the bottom two Ru layers were fully relaxed until the net force was smaller than  $0.01$  eV Å<sup>-1</sup>. STM images were simulated based on the Tersoff–Hamann approximation.<sup>[42]</sup>

**Non-Contact Atomic Force Microscopy:** The non-contact AFM (nc-AFM) measurements were conducted at  $4.2$  K with a base pressure lower than  $2 \times 10^{-10}$  mbar. A commercial qPlus tuning fork sensor in frequency modulation mode with Pt/Ir tip was used to obtain the images. The resonance frequency was about  $27.9$  kHz and the stiffness was about  $1800$  N  $\text{m}^{-1}$ . The STM topography images were acquired in constant-current mode. The constant-height AFM modes were used to measure the real topography features of the  $\text{Si}_9\text{C}_{15}$ .

**Scanning Transmission Electron Microscopy:**  $\text{C}_{60}$  and Sb overlayers were evaporated onto the surface (held at  $200$  K) to protect the  $\text{Si}_9\text{C}_{15}$ /Ru(Rh) from damage during the cross-sectional sample preparation process. Then, electron-transparent lamellas for STEM investigation were prepared by conventional lift-off focused-ion-beam (FIB) technique using a Thermo Scientific Helios G4 CX DualBeam system, operated at accelerating voltages of  $30$  kV down to  $2$  kV to ensure minimum sample damage. Aberration-corrected STEM characterizations were performed using a Nion HERMES-100, operated at  $60$  kV, and a probe forming semiangle of  $32$  mrad. ABF and HAADF images were acquired using annular detectors with collection semiangles of  $15$ – $30$  and  $75$ – $210$  mrad, respectively. The ABF and HAADF image simulations were obtained using an in-house image simulation package matching the microscope experimental settings described above, and using a supercell with  $15$  nm thickness. It should be noted that the  $\text{Si}_9\text{C}_{15}$  monolayer was easily damaged during either the sample preparation process or electron illumination, and proper experimental conditions were crucial for the STEM analysis. EELS measurements were performed using a collection semiangle of  $75$  mrad, an energy dispersion of  $0.3$  eV per channel, and a probe current of  $\approx 20$  pA. The Si–L ( $99$  eV), C–K ( $283$  eV), and Ru–M ( $279$  eV) absorption edges were integrated for elemental mapping after background subtraction. The parent spectrum image was processed with the principal component analysis (PCA) tool to reduce random noise.

## Supporting Information

Supporting Information is available from the Wiley Online Library or from the author.

## Acknowledgements

The authors thank Sokrates T. Pantelides for critical reading and constructive suggestions about the manuscript. The authors are also grateful to Shixuan Du, Wei Ji, and Chen Liu for helpful discussion. This work was supported by the Ministry of Science and Technology of China (2019YFA0308500, 2018YFA0305700, and 2018YFA0305800), the National Natural Science Foundation of China (61888102, 52072401,

and 51991340), CAS Project for Young Scientists in Basic Research (YSBR-003), the Beijing Outstanding Young Scientist Program (BJJWZY)H01201914430039), and the Fundamental Research Funds for the Central Universities (E1E40209).

## Conflict of Interest

The authors declare no conflict of interest.

## Author Contributions

Z.-Y.G., W.X., Y.G., and R.G. contributed equally to this work. H.-J.G. supervised the project. H.-J.G. and G.L. designed the experiments. Z.-Y.G., W.P.X., X.Y.W., X.L., Q.H., and G.L. synthesized Si<sub>9</sub>C<sub>15</sub> and performed the STM experiments. Z.-Y.G. and H.G. performed the XPS experiments. Q.Z. performed the AFM experiments. Y.X.G., Y.-Y.Z., and L.Z.Z. performed the DFT calculations. R.G., Z.L.Z., and W.Z. performed the STEM experiments. Z.-Y.G., Y.X.G., L.Z.Z., G.L., W.Z., and H.-J.G. analyzed the experimental data with inputs from all other authors. All authors participated in writing the manuscript.

## Data Availability Statement

The data that support the findings of this study are available from the corresponding author upon reasonable request.

## Keywords

2D materials, air-stable materials, honeycomb structures, Si<sub>9</sub>C<sub>15</sub> monolayers, Si<sub>x</sub>C<sub>y</sub>

Received: May 27, 2022

Revised: June 29, 2022

Published online:

- [1] K. S. Novoselov, A. K. Geim, S. V. Morozov, D. Jiang, Y. Zhang, S. V. Dubonos, I. V. Grigorieva, A. A. Firsov, *Science* **2004**, *306*, 666.
- [2] A. H. Castro Neto, F. Guinea, N. M. R. Peres, K. S. Novoselov, A. K. Geim, *Rev. Mod. Phys.* **2009**, *81*, 109.
- [3] Z. Y. Al Balushi, K. Wang, R. K. Ghosh, R. A. Vilá, S. M. Eichfeld, J. D. Caldwell, X. Qin, Y.-C. Lin, P. A. DeSario, G. Stone, S. Subramanian, D. F. Paul, R. M. Wallace, S. Datta, J. M. Redwing, J. A. Robinson, *Nat. Mater.* **2016**, *15*, 1166.
- [4] G. Li, Y. Y. Zhang, H. Guo, L. Huang, H. Lu, X. Lin, Y. L. Wang, S. Du, H. J. Gao, *Chem. Soc. Rev.* **2018**, *47*, 6073.
- [5] P. Vogt, P. De Padova, C. Quaresima, J. Avila, E. Frantzeskakis, M. C. Asensio, A. Resta, B. Ealet, G. L. Lay, *Phys. Rev. Lett.* **2012**, *108*, 155501.
- [6] L. Meng, Y. Wang, L. Zhang, S. Du, R. Wu, L. Li, Y. Zhang, G. Li, H. Zhou, W. A. Hofer, H. J. Gao, *Nano Lett.* **2013**, *13*, 685.
- [7] B. Feng, J. Zhang, Q. Zhong, W. Li, S. Li, H. Li, P. Cheng, S. Meng, L. Chen, K. Wu, *Nat. Chem.* **2016**, *8*, 563.
- [8] A. J. Mannix, X. F. Zhou, B. Kiraly, J. D. Wood, D. Alducin, B. D. Myers, X. Liu, B. L. Fisher, U. Santiago, J. R. Guest, M. J. Yacaman, A. Ponce, A. R. Oganov, M. C. Hersam, N. P. Guisinger, *Science* **2015**, *350*, 1513.
- [9] L. Li, S. Z. Lu, J. Pan, Z. Qin, Y. Q. Wang, Y. Wang, G. Y. Cao, S. Du, H. J. Gao, *Adv. Mater.* **2014**, *26*, 4820.
- [10] F. F. Zhu, W. J. Chen, Y. Xu, C. L. Gao, D. D. Guan, C. H. Liu, D. Qian, S. C. Zhang, J. F. Jia, *Nat. Mater.* **2015**, *14*, 1020.
- [11] F. Reis, G. Li, L. Dudy, M. Bauernfeind, S. Glass, W. Hanke, R. Thomale, J. Schäfer, R. Claessen, *Science* **2017**, *357*, 287.
- [12] L. J. Zhou, Y. F. Zhang, L. M. Wu, *Nano Lett.* **2013**, *13*, 5431.
- [13] Y. Li, F. Li, Z. Zhou, Z. Chen, *J. Am. Chem. Soc.* **2011**, *133*, 900.
- [14] S. Chabi, K. Kadel, *Nanomaterials* **2020**, *10*, 2226.
- [15] Z. Shi, Z. Zhang, A. Kutana, B. I. Yakobson, *ACS Nano* **2015**, *9*, 9802.
- [16] T. Susi, V. Skakalova, A. Mittelberger, P. Kotrusz, M. Hulman, T. J. Pennycook, C. Mangler, J. Kotakoski, J. C. Meyer, *Sci. Rep.* **2017**, *7*, 4399.
- [17] S. Lin, S. Zhang, X. Li, W. Xu, X. Pi, X. Liu, F. Wang, H. Wu, H. Chen, *J. Phys. Chem. C* **2015**, *119*, 19772.
- [18] S. Chabi, Z. Guler, A. J. Brearley, A. D. Benavidez, T. S. Luk, *Nanomaterials* **2021**, *11*, 1799.
- [19] Y. Pan, H. Zhang, D. Shi, J. Sun, S. Du, F. Liu, H.-j. Gao, *Adv. Mater.* **2009**, *21*, 2777.
- [20] L. Huang, Y. F. Zhang, Y. Y. Zhang, W. Xu, Y. Que, E. Li, J. B. Pan, Y. L. Wang, Y. Liu, S. X. Du, S. T. Pantelides, H. J. Gao, *Nano Lett.* **2017**, *17*, 1161.
- [21] G. Li, H. Zhou, L. Pan, Y. Zhang, L. Huang, W. Xu, S. Du, M. Ouyang, A. C. Ferrari, H. J. Gao, *J. Am. Chem. Soc.* **2015**, *137*, 7099.
- [22] M. Sicot, P. Leicht, A. Zusan, S. Bouvron, O. Zander, M. Weser, Y. S. Dedkov, K. Horn, M. Fonin, *ACS Nano* **2012**, *6*, 151.
- [23] W. J. Arnoult, R. B. McLellan, *Scr. Metall.* **1972**, *6*, 1013.
- [24] X. Xu, J. Zhuang, Y. Du, H. Feng, N. Zhang, C. Liu, T. Lei, J. Wang, M. Spencer, T. Morishita, X. Wang, S. Dou, *Sci. Rep.* **2014**, *4*, 7543.
- [25] Y. Shao, S. Song, X. Wu, J. Qi, H. Lu, C. Liu, S. Zhu, Z. Liu, J. Wang, D. Shi, S. Du, Y. Wang, H. J. Gao, *Appl. Phys. Lett.* **2017**, *111*, 113107.
- [26] G. Li, L. Zhang, W. Xu, J. Pan, S. Song, Y. Zhang, H. Zhou, Y. Wang, L. Bao, Y. Y. Zhang, S. Du, M. Ouyang, S. T. Pantelides, H. J. Gao, *Adv. Mater.* **2018**, *30*, 1804650.
- [27] G. Kremer, J. C. Alvarez Quiceno, S. Lisi, T. Pierron, C. Gonzalez, M. Sicot, B. Kierren, D. Malterre, J. E. Rault, P. L. Fevre, F. Bertran, Y. J. Dappe, J. Coraux, P. Pochet, Y. Fagot-Revurat, *ACS Nano* **2019**, *13*, 4720.
- [28] X. Lin, S. Lin, Y. Xu, A. A. Hakro, T. Hasan, B. Zhang, B. Yu, J. Luo, E. Li, H. Chen, *J. Mater. Chem. C* **2013**, *1*, 2131.
- [29] Q. Zhang, Y. Chen, C. R. Pan, M. Y. Chou, C. Zeng, C. K. Shih, *Nat. Commun.* **2016**, *7*, 13843.
- [30] C.-P. Lu, G. Li, J. Mao, L.-M. Wang, E. Y. Andrei, *Nano Lett.* **2014**, *14*, 4628.
- [31] F. Tumino, C. S. Casari, M. Passoni, V. Russo, A. L. Bassi, *Nanoscale Adv.* **2019**, *1*, 643.
- [32] C. Riedl, C. Coletti, T. Iwasaki, A. A. Zakharov, U. Starke, *Phys. Rev. Lett.* **2009**, *103*, 246804.
- [33] C. Moreno, M. Vilas-Varela, B. Kretz, A. Garcia-Lekue, M. V. Costache, M. Paradinas, M. Panighel, G. Ceballos, S. O. Valenzuela, D. Peña, A. Mugarza, *Science* **2018**, *360*, 199.
- [34] L. Tao, E. Cinquanta, D. Chiappe, C. Grazianetti, M. Fanciulli, M. Dubey, A. Molle, D. Akinwande, *Nat. Nanotechnol.* **2015**, *10*, 227.
- [35] Q. Li, V. S. C. Kolluru, M. S. Rahn, E. Schwenker, S. Li, R. G. Hennig, P. Darancet, M. K. Y. Chan, M. C. Hersam, *Science* **2021**, *371*, 1143.
- [36] Y. Du, J. Zhuang, J. Wang, Z. Li, H. Liu, J. Zhao, X. Xu, H. Feng, L. Chen, K. Wu, X. Wang, S. Dou, *Sci. Adv.* **2016**, *2*, e1600067.
- [37] Z.-B. Wu, Z.-Y. Gao, X.-Y. Chen, Y.-Q. Xing, H. Yang, G. Li, R. Ma, A. Wang, J. Yan, C. Shen, S. Du, Q. Huan, H.-j. Gao, *Rev. Sci. Instrum.* **2018**, *89*, 113705.
- [38] G. Kresse, J. Furthmüller, *Phys. Rev. B* **1996**, *54*, 11169.
- [39] G. Kresse, J. Furthmüller, *Comp. Mater. Sci.* **1996**, *6*, 15.
- [40] P. E. Blöchl, *Phys. Rev. B* **1994**, *50*, 17953.
- [41] J. P. Perdew, K. Burke, M. Ernzerhof, *Phys. Rev. Lett.* **1996**, *77*, 3865.
- [42] J. Tersoff, D. R. Hamann, *Phys. Rev. B* **1985**, *31*, 805.